# Modeling of shear failure in fractured reservoirs with a porous matrix

Comput Geosci (2017) 21:1119–1134
DOI 10.1007/s10596-017-9680-x

ORIGINAL PAPER

# Modeling of shear failure in fractured reservoirs with a porous matrix

**Rajdeep Deb**[1] · **Patrick Jenny**[1]

Received: 30 September 2016 / Accepted: 26 June 2017 / Published online: 19 July 2017


**Abstract** A finite volume-based numerical modeling framework using a hierarchical fracture representation (HFR) has been developed to compute flow-induced shear failure. To accurately capture the mechanics near fracture manifolds, discontinuous basis functions are employed which ensure continuity of the displacement gradient across fractures. With these special basis functions, traction and compressive forces on the fracture segment can be calculated without any additional constraints, which is extremely useful for estimating the irreversible displacement along the fracture (slip) based on a constitutive friction law. The method is further extended to include slip-dependent hydraulic aperture change and grid convergent results are obtained. Further, the change in hydraulic aperture is modeled using an asymptotic representation which respects the experimentally observed behavior of pore volume dilation due to shear slip. The model allows the initial rapid increase in hydraulic aperture due to shear slip and asymptotically approaches a finite value after repeated shearing of a fracture segment. This aperture increase is the only feedback for mechanics into the fluid flow for a linear elastic mechanics problem. The same model is also extended to include poroelastic relations between flow and mechanics solver. The grid convergence result in the case of poroelastic flow-mechanics coupling for flow-induced shear failure is also obtained. This proves the robustness of the numerical and analytical modeling of fracture and friction in the extended finite volume method (XFVM) set-up. Finally, a grid convergent result for seismic moment magnitude for single fracture and fracture network with random initial hydraulic and friction properties is also obtained. The *b*-value, which represents the slope of seismic moment occurrence frequency decay vs seismic moment magnitude, which is approximately constant in a semi-logarithmic plot, is estimated. The numerical method leads to converged *b*-values for both single fracture and fracture network simulations, as grid and time resolutions are increased. For the resulting linear system, a sequential approach is used, that is, first, the flow and then the mechanics problems are solved. The new modeling framework is very useful to predict seismicity, permeability, and flow evolution in geological reservoirs. This is demonstrated with numerical simulations of enhancing a geothermal system.

**Keywords** Slip · Aperture · Friction · XFVM

## 1 Introduction

The geological domain of a typical deep geothermal reservoir is characterized by low matrix and fracture permeability, and therefore, fracturing via high-pressure fluid injection is required prior to energy extraction. Such permeability enhancements occur due to flow-induced shear slip along existing fracture manifolds and are crucial for the creation of enhanced geothermal systems (EGS). The micro-seismicity resulting from these shear failure events is an important observation and plays a role in managing both creation and operation of EGS. The termination of the operations in Basel (2006) is an example of how public perceptions can hinder the development of EGS plants due to seismic concerns. Here, improved simulation capabilities play a vital role in order to make qualified decisions.

✉ Rajdeep Deb
debr@ethz.ch

[1] Institute of Fluid Dynamics, ETH Zurich, Sonneggstrasse 3, 8092, Zurich, Switzerland

The geological domains contain fractures of different lengths and orientations. Further, the physical properties such as aperture, friction coefficients, and modulus of elasticitiy vary over many orders of magnitude. In the presence of matrix porosity, there exists a further flow-mechanics coupling in the poroelastic fractured geological domain. Efficient numerical modeling of such poroelastic, heterogeneous, fractured reservoirs is a challenging task. A number of methods such as boundary element methods, displacement discontinuity methods, and fast multipole methods have been proposed in the literature to deal with mechanics simulations of fractured networks. All these methods work on the fracture degrees of freedom (dof) only. Limitations of such methods arise in the case of heterogeneous physical properties and if long-distant intereactions between fractures are important, e.g., in the case of poroelastic media. However, computing the full matrix-fracture interaction by adapting the grid around the fractures is a computationally very expensive process. A compromise between solving only for fracture dof and resolving the full matrix-fracture interaction is to use a hierarchical fracture representation (HFR) model. In this approach, large fractures are represented as lower dimensional manifolds embedded in a higher dimensional matrix. The mathematical equations governing the fluid flow problem in such approximate models is modified to include a consistent mass transfer term between fracture and matrix [1]. A number of numerical methods for fluid flow solver in the context of HFR have been developed over the last decade [2, 3]. The research in developing a numerical mechanics solver for such HFR is relatively new. In this regard, one methodology is to use special discontinuity basis functions to resolve shear slip in the embedded fractures [4–7]. The extended finite element method (XFEM) is one such strategy. Another recently developed approach is to use a finite volume method and discontinuity basis functions to account for shear slip along the fracture manifold and the stress perturbations in the nearby matrix domain. In a recently submitted paper by Deb and Jenny [8], this method is further described and is called extended finite volume method (XFVM). It was applied in the context of one-way coupling problems, where fluid pressure induces shear slip. A more general method would also account for changes in fracture aperture due to shear slip, but obtaining grid-converged solutions for such scenarios is difficult. In this paper, generalized two-way coupling between flow and mechanics, both in fracture and matrix domains, is considered. The poroelastic coupling between flow and mechanics in the matrix is based on a fixed stress approach [9]. The hydraulic aperture dilation due to shear slip is modeled using an asymototic approach, where the properties of initial rapid aperture change and the slower changes occurring at a later stage are honored [10].

Section 2 describes the governing equations for flow, transport, and mechanical equilibrium along with the models for friction and aperture. The numerical methods of XFVM and poroelastic coupling are described in the Section 3. Results of studies with a single fracture and a fracture network are presented in Section 4. Finally, in Section 5, benefits of the new modeling approach are discussed.

## 2 Problem description

### 2.1 Governing equations for mechanics

A fractured reservoir can be approximated as a poroelastic domain with fractures, which have a maximum shear strength. The fractures can bear a maximum shear, beyond which slip occurs resulting in micro-seismic events. The equilibrium of such fractured domains may be disturbed by increasing the fluid pressure or by changing the boundary conditions, which both can lead to shear failure. Force balance in an unit volume of the continuum is described by the equation below:

$$\nabla \cdot \left( \tilde{\sigma} - bp\tilde{I} \right) + \mathbf{f} = 0, \tag{1}$$

where the terms $\tilde{\sigma}$, $p$, and $\mathbf{f}$ respectively represents the effective stress tensor field, local fluid pressure, and the body force due to gravity. The terms $b$ and $\tilde{I}$ respectively denote Biot coefficient and identity tensor. The effective stress $\tilde{\sigma}$ is obtained as follows:

$$\tilde{\sigma} = \lambda(\nabla \cdot \mathbf{u})\tilde{I} + G(\nabla \mathbf{u} + \nabla \mathbf{u}^T). \tag{2}$$

In Eq. 2, the effective stress $\tilde{\sigma}$ is linearly dependent on bulk strain $(\nabla \cdot \mathbf{u})\tilde{I}$ and total strain $\frac{1}{2}(\nabla \mathbf{u} + \nabla \mathbf{u}^T)$. The proportionality constants are respectively the first Lamé constant $\lambda$ and the second Lamé constant or shear modulus $G$. It is important to note that Eq. 1 is obtained after neglecting the acceleration term in the dynamic force balance problem. This is an important assumption in order to efficiently obtain numerical solutions for fluid injection-induced shear failures. The assumption to neglect the mechanical wave propagation timescale for shear failure is related to the larger timescale of the fluid flow process in the case of a fractured reservoirs. Since the flow influences the shear failure by reducing the compressive stress on the fracture segments, it is important to verify that all the shear and compressive wave propagation timescales across the reservoir is much smaller than the flow propagation timescale in the fractures. The finite volume-based numerical solution of the displacement field $\mathbf{u}$ honors force balance in each finite volume. Using Eq. 2, this solution also provides the stress field, from which effective compressive stress and shear

traction on each of the fracture segments can be calculated as follows:

$$\sigma_c = -\hat{n} \cdot (\tilde{\sigma} \cdot \hat{n}) \tag{3a}$$

$$\text{and} \qquad \tau = (\tilde{I} - \hat{n}\hat{n}) \cdot \tilde{\sigma} \cdot \hat{n}, \tag{3b}$$

respectively. Note that $\sigma_c$ and $\tau$ are defined with respect to the local coordinate axes normal and parallel to the fracture manifold. The unit vector normal to the fracture manifold is denoted by $\hat{n}$.

### 2.2 Shear failure modeling

The shear failure criterion of a fracture segment can be given as follows:

$$|\tau| \geq S_0 + \mu_s(\sigma_c - p^f), \tag{4}$$

where $p^f$ represents the local fluid pressure at the fracture segment. The coefficients $\mu_s$ and $S_0$ respectively represent the static friction coefficient and cohesive force. Once condition (4) is reached, shear failure occurs leading to irreversible displacement along the fracture manifold, and finally, a new equilibrium solution gets established with traction force on the fracture segment constraint to a new value. Accordingly, the stress field in the neighborhood of the fracture segment gets rearranged to satisfy the constraint on the failed fracture segment. A simple model for this constraint value comes from the Coulomb law. An alternative and experimentally verified approach is to apply a limit for the maximum shear value at the fracture segment [11]. This model is known as Prakash and Clifton [12] law, where the maximum shear value relaxes with decreasing compressive stress over a finite timescale. Further, when it reaches the shear value of the fracture segment, the fracture slips in such a way that the new solution of fracture shear is constraint to this maximum shear value. This allows for regularization of the shear slip solution and therefore grid independence for dynamic failure simulations [13]. In the context of pressure-induced shear failure, the timescale of shear maximum relaxation due to decreasing compressive stress should be in the order of the flow timescale [8]. Relaxation of the maximum shear value is modeled as follows:

$$\frac{d\tau_{\max}}{dt} = -\frac{1}{t_f}(\tau_{\max} - \mu_s(\sigma_c - p^f)), \tag{5}$$

where $t_f$ represents the shear relaxation timescale, which is of the order of flow timescale and is crucial for grid convergence. In Eq. 5, the term $\tau_{\max}$ represents the shear strength at the fracture segment.

### 2.3 Governing equations for fluid flow

In the set-up of fractures embedded in a damaged matrix, large fractures are represented discretely, while small fractures are approximated by an effective matrix permeability. The HFR leads to the following set of equations for mass balance in the fractures and the damaged matrix:

$$\frac{\partial E^f}{\partial t} - \nabla_f \cdot \left( \frac{b^f \boldsymbol{\kappa^f}}{\mu} \cdot (\nabla_f p^f - \rho \mathbf{g}) \right) + \Psi^{f \to m} = q^f \tag{6}$$

$$\text{and} \quad \frac{\partial \phi^m}{\partial t} - \nabla \cdot \left( \frac{\boldsymbol{\kappa^m}}{\mu} \cdot (\nabla p^m - \rho \mathbf{g}) \right) + \Psi^{m \to f} = q^m. \tag{7}$$

The operator $\nabla_f$ represents the gradient along fracture manifolds. The variables in Eq. 6 are pore volume per unit fracture area given as $E^f$ (void aperture), hydraulic aperture $b^f$, fracture permeability tensor $\kappa^f$, fluid viscosity $\mu$, fracture pressure $p^f$, fluid density $\rho$, gravitational accelaration vector $\mathbf{g}$, and the well injection rate $q^f$. The variables in Eq. 7 are matrix porosity $\phi^m$, matrix permeability tensor $\kappa^m$, matrix pressure $p^m$, and the well injection rate $q^m$. The change in volumetric strain ($\nabla \cdot \mathbf{u}$) due to stress in the damaged matrix leads to a change in porosity $\phi^m$ and therefore affects mass balance. On the other hand, fluid pressure leads to a change of volumetric stress and therefore of the stress field in the fractured domain. Neglecting the effect of gravity in Eq. 7, the coupled flow and mechanics equations for the matrix domain can be expressed as follows:

$$\nabla \cdot \left( \tilde{\sigma} - b p^m \tilde{I} \right) + \mathbf{f} = 0 \tag{8}$$

$$\text{and} \quad \frac{1}{M}\frac{\partial p^m}{\partial t} + b\frac{\partial (\nabla \cdot \mathbf{u})}{\partial t} - \nabla \cdot \left( \frac{\boldsymbol{\kappa^m}}{\mu} \cdot \nabla p^m \right) + \Psi^{m \to f} = q^m, \tag{9}$$

where $M$ and $b$ are Biot modulus and Biot coefficients, respectively. Consistent, detailed formulations of fracture to matrix ($\Psi^{f \to m}$) and matrix to fracture ($\Psi^{m \to f}$) mass transfer terms are given in [3] and [2].

### 2.4 Modeling of slip dilation

Shear slip leads to an increase of hydraulic and void aperture. Various modeling approaches are used to obtain a relation between shear slip and aperture change. In general, aperture change as a function of shear slip follows an initial rapid change and then a slower increase. McClure and Horne [14] used the following set of equations to determine hydraulic and void aperture changes:

$$b^f = b_0^f + \beta_1 s_1 + \beta_2 s_2 \tag{10}$$

$$\text{and } E^f = E_0^f + \left( \frac{E_a}{(1 + (9(\sigma_c - p^f)/\sigma_{\text{nref}}))} \right) + \beta_1 s_1 + \beta_2 s_2. \tag{11}$$

In Eqs. 10 and 11, terms $\beta_1$ and $\beta_2$ respectively accounts for initial rapid and later slower dilation rate due to shear slip.

The corresponding variables $s_1$ and $s_2$ denote the initial and later slip accumulations of a fracture segment. The terms $b_0^f$ and $E_0^f$ denote the initial hydraulic and void aperture, respectively. The terms $E_a$ and $\sigma_{\text{nref}}$ are material constants. A better approach is one in which the aperture asyomtotically dilates to a fixed value after repeated shear failure of a fracture segment. The experimental observation for pore volume dilation suggests a model which has initial sharp rise in aperture with shear slip and later saturates to a constant value after repeated shear slip [10]. Here, the exponential model

$$b^f = b_0^f + \Delta b(1 - \exp(-s/s_0)) \tag{12}$$

is employed which honors such criterion. Equation 12 is charactrized by the final asyomtotic increase $\Delta b$ and the sensitivity $s_0^{-1}$. The variable $s$ denotes the total cumulative shear slip since the beginning of fluid injection-induced shear failure on a fracture segment. The aperture dilation is rapid for $s \ll s_0$ and is very slow, if $s \gg s_0$. The continuous and differentiable behavior of this model provides a smooth transition between initial and later stages of shear slip, which is also beneficial for the numerical solution algorithm.

## 3 Numerical methods

### 3.1 Fracture representation and XFVM

Using discrete fracture manifolds embedded in a matrix domain is an efficient way to describe fractured reservoirs without adapting the grid around the fractures. A recently submitted paper by Deb and Jenny [8] describes how the finite volume method can be used to accurately resolve the displacement solution and shear slip around fractures. The method is named XFVM, in which discontinuity basis functions around embedded fractures are used to resolve the shear slip. The method is similar to XFEM in the sense that discontinuity basis functions are used to represent shear slip. The main difference is that as compared to XFEM, the locations of the discontinuity dof coincide with the additional fracture nodes. The basis functions completely respect fracture orientation and location irrespective of the grid around the fracture. In the case of a constant irreversible jump across a fracture segment, the corresponding correction of the strain in the matrix domain is obtained from the discontinuity basis function at the fracture segment and the shear slip dof. Further details of how shear slip affects the discretized strain calculation is described in Appendix 1. In the case of shear failure, an additional constraint for the frictional constitutive relation is solved to get the slip along with the force balance equations for the matrix node dof. Therefore, once the failure criterion is reached for a fracture segment, the constraint relation

$$\int_0^L \tau dL = \int_0^L \tau_{\max} dL \tag{13}$$

has to be honored for the fracture segment, in addition to the force balance equation

$$\int_{d\Omega} \left(\tilde{\sigma} - bp\tilde{I}\right) \cdot d\mathbf{A} + \int_{\Omega} \mathbf{f} d\Omega = 0 \tag{14}$$

in each of the finite volumes $\Omega$. Here, $L$ is the length of the fracture segment and $\tau_{\max}$ its shear strength. The coupled Eqs. (13) and (14) are solved to obtain the new displacement field and therefore the stress solution. Coupling of matrix and fracture equilibrium solutions takes care of distant interactions between fractures and matrix domains. For example, the matrix force balance (14) is elliptic in nature, and therefore, any perturbation due to shear failure in one of the fractures influences the displacement field in the entire domain. In the XFVM method, a bilinear basis function is associated with each discretization node in the matrix domain. The displacement field is now approximated as follows:

$$\mathbf{u} \approx \sum_{I=1}^{N_e} \mathbf{u}_I N_I(\mathbf{x}) + \sum_{j=1}^{N_s} \mathbf{s}_J N^J(\mathbf{x}) \tag{15}$$

with

$$N^J(\mathbf{x}) = \left( \sum_{p=1}^{N_e} N_p^J(\mathbf{x}) H_p^J(f^J(\mathbf{x})) \right), \tag{16}$$

$$\text{where } H_p^J(f^J(\mathbf{x})) = H(f^J(\mathbf{x})) - H(f^J(\mathbf{x_p^J})). \tag{17}$$

Figure 1 depicts the dof of fracture and matrix nodes in the interaction region of a fracture manifold and the neighboring matrix domain. The green and red nodes here respectively store the displacement solutions for the matrix domain, slip discontinuity and fluid pressure along the fracture manifold. In Eq. 15, the terms $\mathbf{u}_I$, $N_I$, $\mathbf{s}_J$, and $N^J$ respectively represent the dof for displacement at each finite volume node, the basis function corresponding to the node, the dof for slip at each of the fracture segments, and discontinuous basis functions corresponding to each fracture segment. The terms $N_e$ and $N_s$ represent the number of matrix nodes and fracture dof, respectively. Figure 2 depicts the full discontinuity basis function $N^J(\mathbf{x})$ (on the right) and the contributions $N_p^J(\mathbf{x}) H_p^J(f^J(\mathbf{x}))$ by each neighboring node (on the left). The term $f^J(\mathbf{x})$ represents the distance function of a point $\mathbf{x}$ to the fracture manifold. The function $H(\cdot)$ represents the heaviside function.

### 3.2 Coupling with poro-mechanics

The poro-mechanics of the matrix leads to the full coupling of flow and mechanics at every instant in the whole matrix domain.

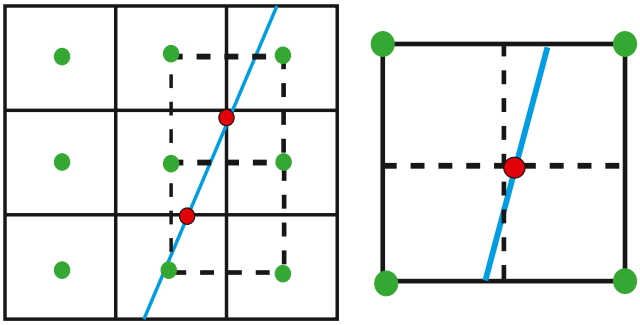

**Fig. 1** The *left* figure shows a stencil involving both matrix and fracture dof. Depicted on the *right* is a single fracture segment with its four neighboring matrix nodes

This requires solving a coupled flow-mechanics problem each timestep in order to obtain correct stress and pressure fields. Efficient solution algorithms are given by [9] and [15], in which a fixed stress approach is used in the sequential mechanics and flow solver. The latter is also used here and coupled with shear failure calculations for the fractured reservoir with embedded fracture representation. As given in the reference [15], iterative update of the pressure field after the mechanics computation is performed such that volumetric stress is conserved over the iteration. This is achieved by solving the following:

$$\int b\nabla\cdot\mathbf{u}_{K+1}^{n+1}dV=\int\left(b\nabla\cdot\mathbf{u}_{K}^{n+1}+\frac{b^2}{K_v}\left(p_{K+1}^{n+1}-p_{K}^{n+1}\right)\right)dV \tag{18}$$

for $p_{K+1}^{n+1}$, where $K_v$ denotes the bulk modulus of elasticity. Note that the superscript $n$ denotes the timestep and the subscript $K$ the iteration.

### 3.3 Role of aperture modeling in timestep selection

The choice of an aperture model such as (12) is also important in order to obtain grid convergent slip solution. The shear strength of a fracture segment without the relaxation criterion can be modeled using the Coulomb friction law as follows:

$$\tau_{\max}=S_0+\mu_s(\sigma_c-p^f). \tag{19}$$

The above equation clearly depicts that the timescale of failure propagation along the fracture manifold depends on the flow propagation timescale, if the boundary conditions are fixed. Based on the grid spacing $\Delta x_f$, $b_f$, $\mu$, and $E^f$, the flow propagation timescale can be estimated as follows:

$$T^{\text{flow}}=\left(12\Delta x_f^2\mu/(b^f)^3\right)\frac{\partial E^f}{\partial p^f}. \tag{20}$$

In the above equation, the cubic law is used to relate the fracture permeability to the hydraulic aperture. In order to obtain grid convergent solutions for shear slip, the choice of the flow timestep size ($\Delta t$) has to satisfy

$$\Delta t<T^{\text{flow}}. \tag{21}$$

The flow timescale $T^{\text{flow}}$ has an inverse cubic dependence on the hydaulic aperture. The shear slip increases the hydraulic aperture and therefore leads to a decrease in the flow propagation timescale. This further reduces the flow timestep size, which has to be small enough to resolve the pressure-dependent failure criterion. Further, in the case of relaxation model (5), the relaxation timescale ($t_f$) of the fracture segments has to be in the order of the flow timescale. The increase in fracture aperture therefore also leads to a decrease in $t_f$. An upper bound on the hydraulic aperture obtained from model (12) provides a lower bound for $T^{\text{flow}}$, and therefore, the choice of maximum timestep size given by Eq. 20 can be obtained. On the other hand,

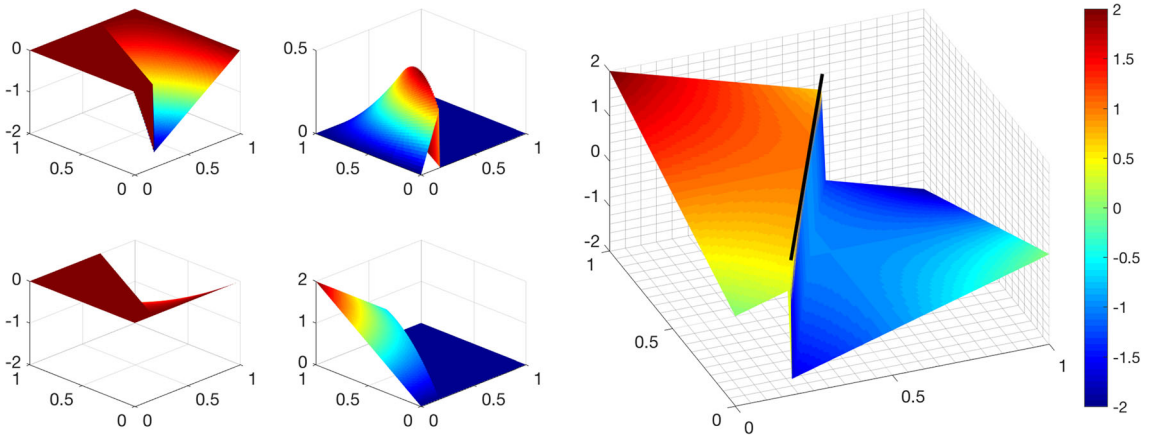

**Fig. 2** The *left* figures represent the contributions to the total discontinuity basis function by each neighboring node. The *right* figure represents the full discontinuity basis function

models such as (10) cannot provide an upper bound for slip-dependent aperture change. This therefore does not gaurantee grid convergent solutions for any choice of timestep size. With model (12) for hydraulic aperture change and a timestep size resolving $t_f$ and $T^{\text{flow}}$ in the cases with relaxation and without relaxation model respectively, grid convergence of slip and pressure is guaranteed.

## 4 Results

### 4.1 Single fracture with damaged matrix

A single fracture embedded in a damaged matrix is considered. The problem set-up is depicted in Fig. 3. Total stress boundary conditions are applied and the fracture is oriented at an angle of 45° with respect to the system coordinates. Permeable matrix domain is considered and constant pressure boundary conditions are applied for the flow. The parameter values for the simulations are provided in Table 1 and simulations are performed to obtain numerical solutions of shear slip, pressure, and aperture along the fracture. In Table 1, the terms $\sigma^r_{yy}$ and $\sigma^r_{xx}$ denote the components of total stress tensor along the horizontal and vertical boundary lines, respectively. The numerical time step of flow simulation is 10 s and the friction relaxation timescale ($t_f$) is 100 s. This numerical timestep, therefore, well resolves the relaxation process of drop in shear strength due to propagating fluid pressure front along the fracture manifold. As a result, the obtained solution for shear slip propagation front and shear traction on the fracture manifold shows the grid convergent behavior as demonstrated in Fig. 4. The Fig. 4 depicts results for slip (top left), shear traction (top right), fluid pressure (bottom left), and fracture aperture (bottom right) for two grid resolutions. In these simulations, void aperture only varies with fluid pressure in the fracture and is modeled by Eq. 11 with $\beta_{1,2} = 0$. The main difference between simulations performed in this section and in the previously submitted paper of Deb and Jenny [8] is that the change in hydraulic aperture due to shear failure is modeled here. The grid convergent result for shear slip and shear traction in this slip front propagation problem under fluid injection depicts that the combination of XFVM and shear relaxation method works well numerically in this two-way coupled set-up.

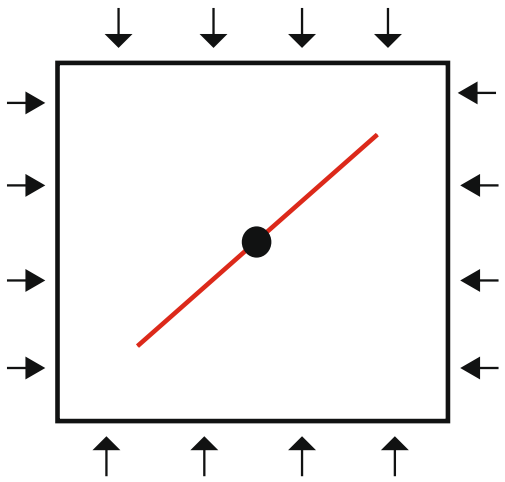

**Fig. 3** The problem set-up with a single fracture embedded in a damaged matrix with stress boundary conditions

The evolution of shear strength ($\tau_{\max}$) and shear stress ($\tau$) for a single point is observed in the left plot of Fig. 5. Fluid injection in the fracture leads to increasing pressure and therefore to a decrease of Coulomb stress (CS), which is defined as follows:

$$\text{CS} = \mu_s(\sigma_c - p^f). \tag{22}$$

The shear strength relaxes to the CS with a timescale of $t_f = 100$ s. The shear stress remains constant unless it becomes equal to shear strength. The shear slip, depicted in the right plot of Fig. 5, constrains the shear stress to the shear strength. The central plot of the Fig. 5 depicts the normal stress ($\sigma$), fluid pressure ($p^f$), and effective normal stress ($\sigma_c$). It is observed that the normal stress on the fracture segment is unaffected by the shear slip. Shear failure also leads to seismic events. A common way to present micro-seismic statistics is to plot the occurrence frequency of slipping events against the seismic moment magnitude ($M_w$). The latter is defined as follows:

$$M_w = \frac{2}{3}\log\left(GA_{3d}\sum|\triangle s_i|\right) - 6.06, \tag{23}$$

according to [16]. Here, SI units are used for all the parameters in Eq. 23. Note that $|\triangle s_i|$ is the slip displacement

**Table 1** The values of different parameters used in the simulations

| Variable name | Value | Variable name | Value |
|---|---|---|---|
| $p^{m,f}_{init}$ | 40 MPa | $t_f$ | 100 s |
| $\sigma^r_{xx}$ | 70 MPa | $\sigma_{\text{Enref}}$ | 95 MPa |
| $\sigma^r_{yy}$ | 50 MPa | $\mu_s$ | 0.6 |
| $G$ | 10 GPa | $\lambda$ | 2.5 GPa |
| $E^f_0$ | 1 mm | $S_0$ | 0 |
| $b^f_0$ | 0.1 mm | $(A_{3d}/L)$ | 100 m |
| $\mu$ | $8.9 \times 10^{-4}$ Pa.s | $\kappa^m$ | $10^{-14}m^2$ |
| $\Delta b$ | 0.5 mm | $s_0$ | 20 mm |
| $t_0$ | 100 s | $\sigma_f$ | 1 |
| $b_0$ | 0.5 mm | $\sigma_b$ | 0.3 mm |
| $\mu_a$ | 0.55 | $\mu_b$ | 0.65 |
| $b$ | 0.44 | $M$ | 100 GPa |
| $E_a$ | 1 mm | | |

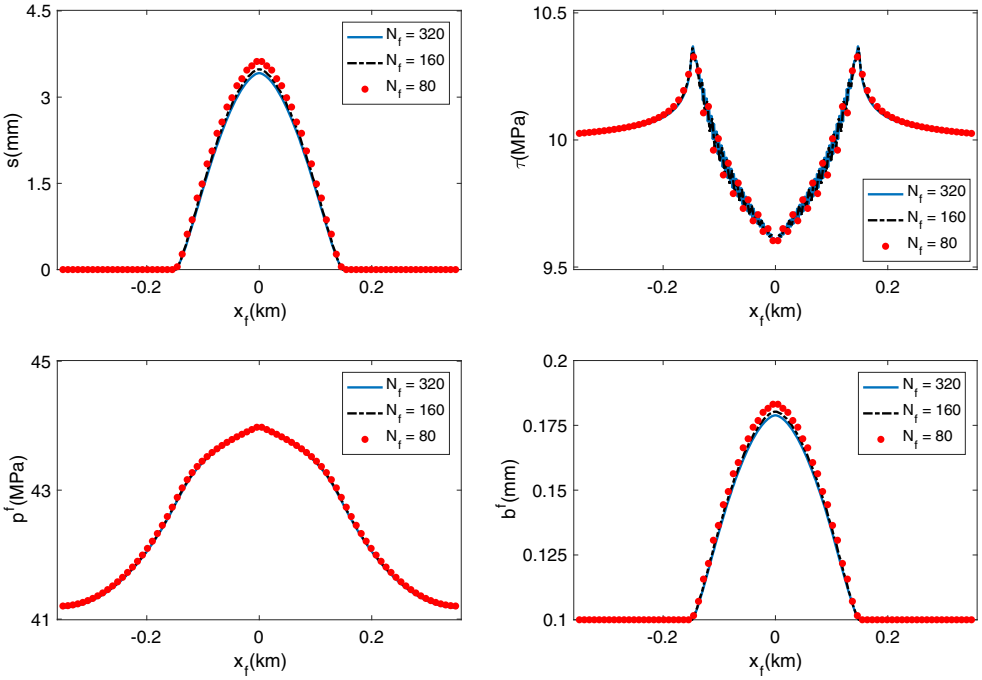


**Fig. 4** Simulation results with a single oblique fracture embedded in an impermeable 2-D square matrix domain obtained with three different grid resolutions, that is, with 80, 160 and 320 fracture segments: cumulative slip (*top left*), shear traction (*top right*), fracture fluid pressure (*bottom left*), and fracture aperture (*bottom right*) along the fracture after 3500 s

magnitude of fracture segment $i$ with area $A_{3d}$ during a specified seismic shear slip event. Here, $A_{3d}$ represents the area of the fracture segment, and since the 2D surface represents a slice with a thickness of 100 m, the area $A_{3d}$ of a fracture segment with length $L$ (in meter) is 100 L m$^2$. Note that the sum involves all segments, which fail at the same time and form a connected patch. We define this plot as $b$-value curve in the rest of the paper. The two plots in Fig. 6 depict the $b$-value curves for two different grid (left figure) and time resolutions (right figure). In the $b$-value curves, the term $N_v$ represents the number of events with moment magnitude greater than $M_w^v$ normalized by the total number of events. The curves are linear in the semi-logarithmic plot, essentially grid-independent, and in agreement with the Gutenberg-Richter law. The slope of these linear lines is described as $b$-value.

### 4.2 Single fracture with poroelastic matrix

The single fracture test case discussed in the previous section is used here with an additional feature of poroelastic coupling in the matrix domain. In order to resolve the flow-mechanics coupling in the matrix domain, the fixed stress approach is used [9]. The XFVM numerical solver for the fracture domain shear failure, the shear strength relaxation model (5), and hydraulic aperture change model (12) has been used. The boundary conditions and the injection well location are the same as in the previous test case, but the fluid is injected at 45 MPa and the initial fluid pressure is 40 MPa everywhere. Biot coefficient ($b$), Biot modulus ($M$), and matrix permeability ($\kappa^m$) are 0.44, 100 GPa, and $10^{-14}$ $m^2$, respectively, and initial hydraulic and void aperture are 1 mm. The grid-converged simulation results for

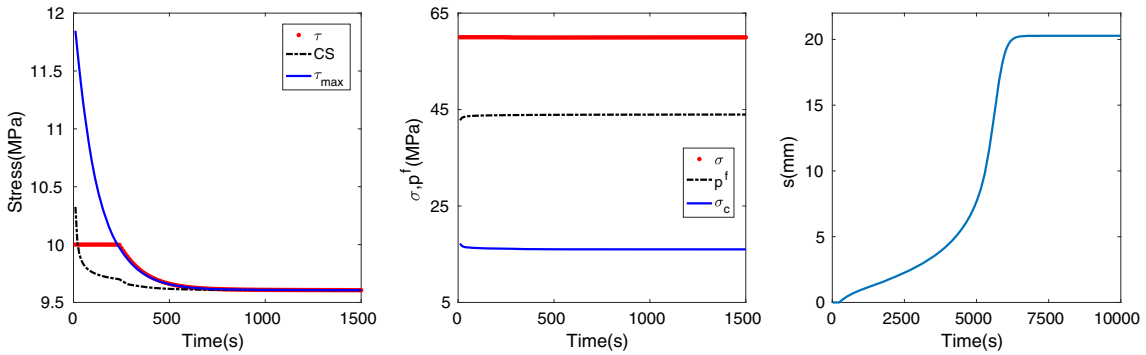


**Fig. 5** Time-dependent solutions at the domain center for the test case with one fracture embedded in an impermeable matrix. Shear stress, normal stress, and slip are shown in the *left*, *middle*, and *right* plots, respectively

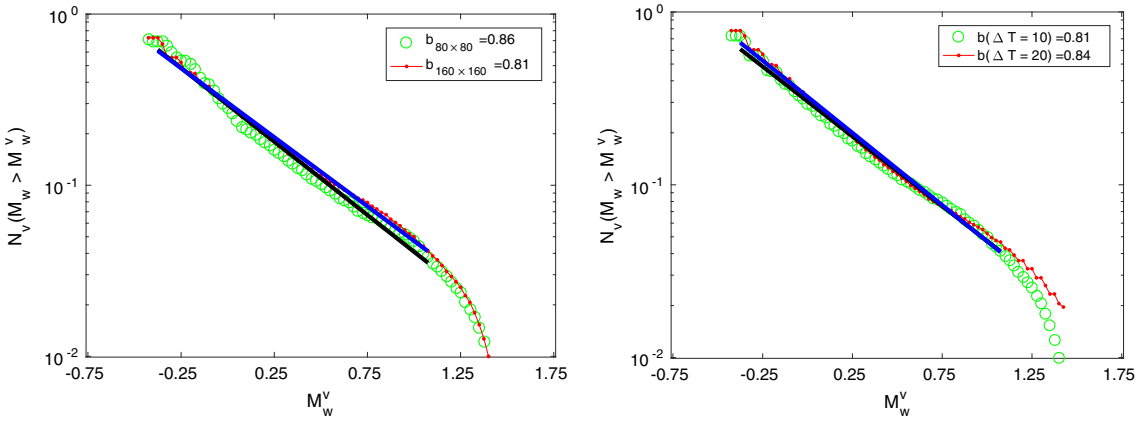


**Fig. 6** The number of events with moment magnitude greater than $M_w^v$ normalized by the total number of events is plotted against the moment magnitude value of $M_w^v$. The *left* plot depicts the curve along with the *b*-value solutions for different grid resolutions of a single fracture. The *right* plot compares the *b*-value solutions of a single fracture for two different time resolutions of flow simulation

slip (top left), shear traction (top right), fracture fluid pressure (bottom left), and fracture aperture (bottom right) are depicted in Fig. 7. The maps in Fig. 8 show the fluid pressure in the matrix (top left), displacement in horizontal (top center), and vertical (top right) directions, and the stress tensor components $\sigma_{xy}$, $(\sigma_{xx} - bp^m)$, and $(\sigma_{yy} - bp^m)$ (bottom) after 350 s. The simulation result depicts that the matrix fluid pressure ($p^m$) increases in the region around the fracture. The shear slip leads to a discontinuity across the region of shear failure for displacement components $u_x$ and $u_y$. In the neighborhood of fracture without any shear failure, the displacement components are effected by the presence of increased fluid pressure due to poroelastic effect. Stress tensor field is reoriented at the tip of shear failure regions along the fracture. This leads to stress peaks for individual stress tensor components.

The seismic event calculations are best represented by *b*-value curve. The *b*-value curves for a single fracture embedded in a poroelastic domain is depicted on the left of Fig. 9 for two different matrix permeability values. The figure shows that the Gutenberg-Richter law is followed with approximately the same *b*-values for varying matrix permeability. The only difference observed with changing matrix permeability is that the number of seismic event occurence

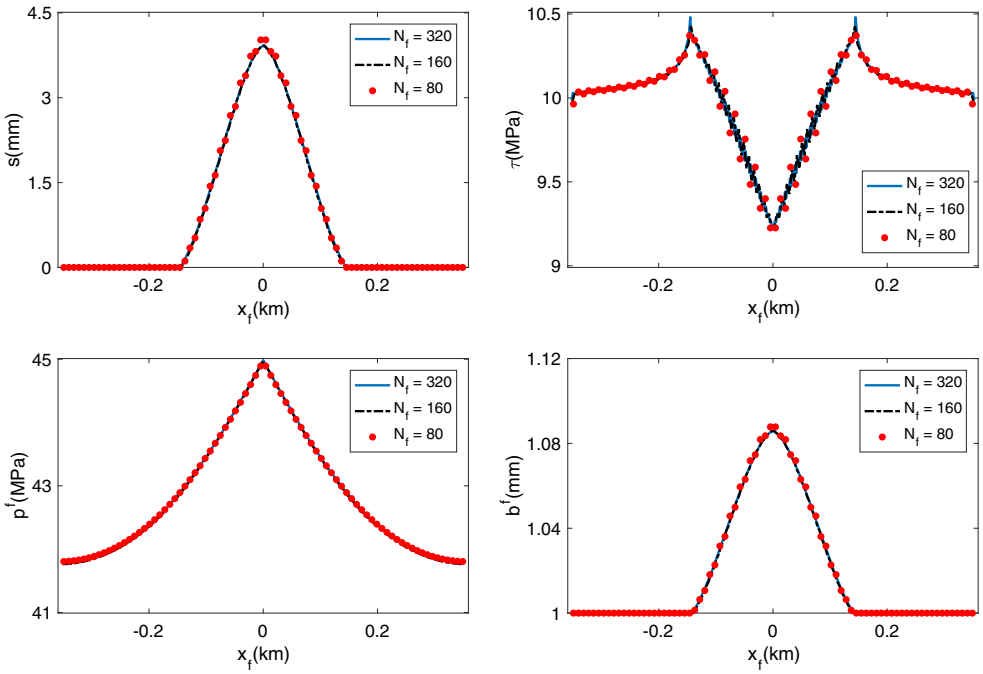


**Fig. 7** Simulation results with a single oblique fracture embedded in a poroelastic 2-D square matrix domain obtained for three different grid resolutions, that is, with 80, 160 and 320 fracture segments: cumulative slip (*top left*), shear traction (*top right*), fracture fluid pressure (*bottom left*), and fracture aperture (*bottom right*) along the fracture after 350 s

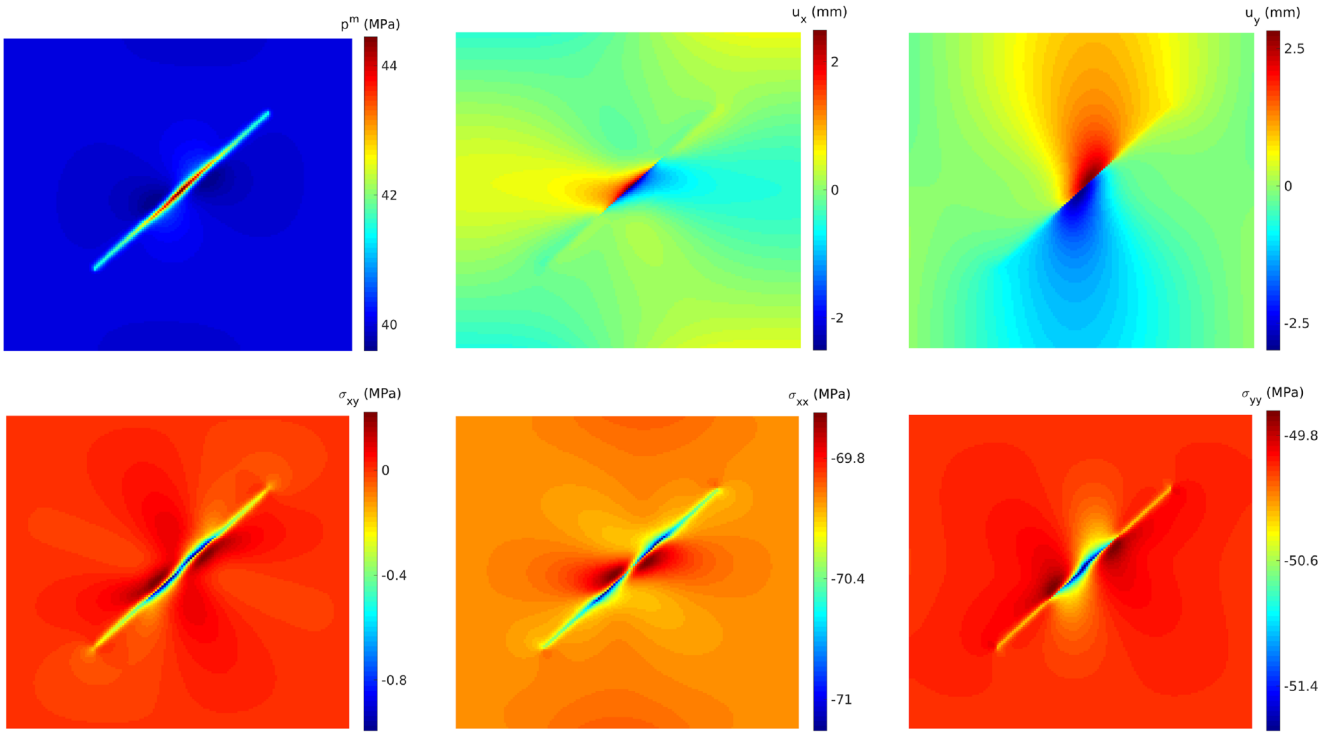


**Fig. 8** Simulation results with a single fracture embedded in a 2-D poroelastic matrix with a permeability of $10^{-14}$ m$^2$ and a Biot coefficient of 0.44. The subfigures show the pressure field (*top left*), displacement in horizontal (*top center*) and vertical (*top right*) directions, and the total stress tensor components $\tilde{\sigma}_{xy}$, $(\tilde{\sigma}_{xx} - bp^m)$, and $(\tilde{\sigma}_{yy} - bp^m)$ (*bottom*) after 350 s

frequency decreases with increasing matrix permeability. This is because with increasing matrix permeability, the mass transfer between fractures and matrix increases, which results in stabilization of the fracture against shear failure due to decreasing fluid pressure along the fracture.

### 4.3 Grid divergence without relaxation

Figure 10 depicts results for slip (top left), shear traction (top right), fluid pressure (bottom left), and fracture aperture (bottom right) using three grid resolutions and without any relaxation modeling approach. Here, the shear strength decays immediately with decreasing compressive stress and is given as follows:

$$\tau_{\max} = \mu_s(\sigma_c - p^f). \tag{24}$$

The numerical timestep used for this simulation is 10 s. With this timestep, the numerical flow propagation timescale obtained for each of the three grid resolutions cannot

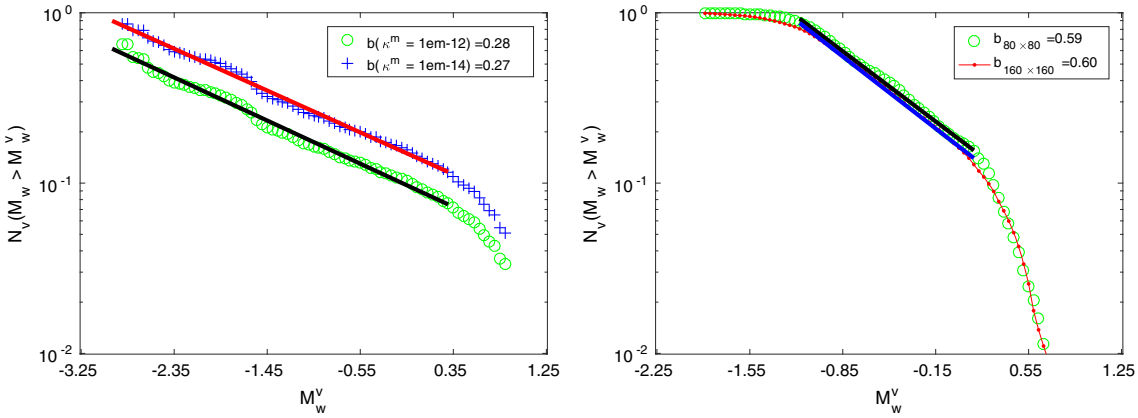


**Fig. 9** The number of events with moment magnitude greater than $M_w^v$ normalized by the total number of events is plotted against the moment magnitude value of $M_w^v$. The *left plot* depicts this seismicity plot for different values of matrix permeability for the poroelastic single fracture. The *right plot* depicts the *b*-value solutions for two different grid resolutions for a linear elastic stochastically generated fracture network domain depicted as *gray lines* in Fig. 11

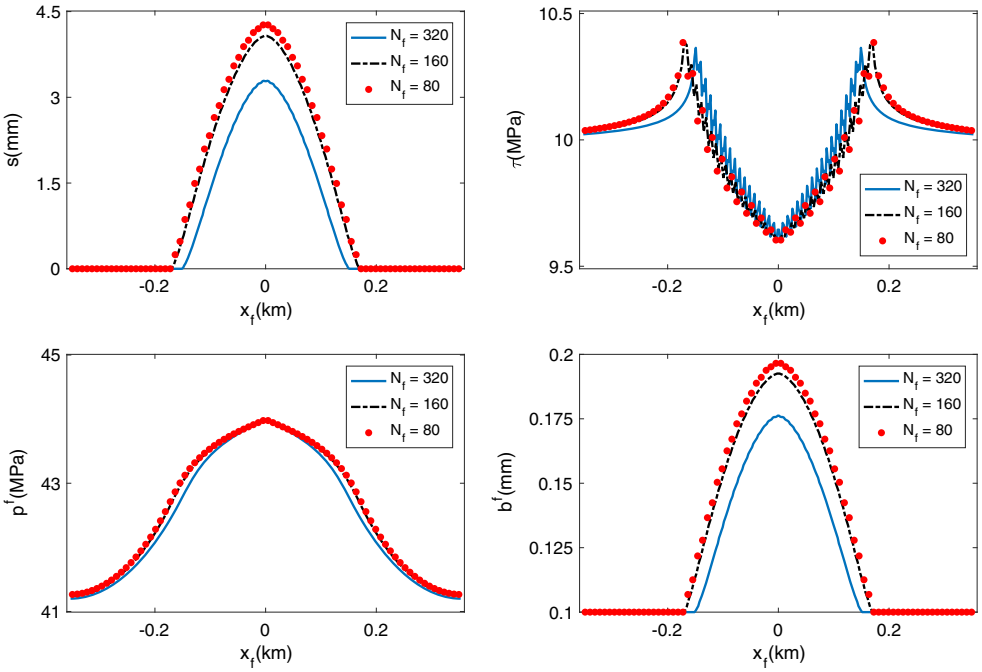


**Fig. 10** Simulation results with a single oblique fracture embedded in an impermeable 2-D square matrix domain obtained with three different grid resolutions, that is, with 80, 160 and 320 fracture segments: cumulative slip (*top left*), shear traction (*top right*), fracture fluid pressure (*bottom left*), and fracture aperture (*bottom right*) along the fracture after 3500 s. No shear strength relaxation timescale is used in this example

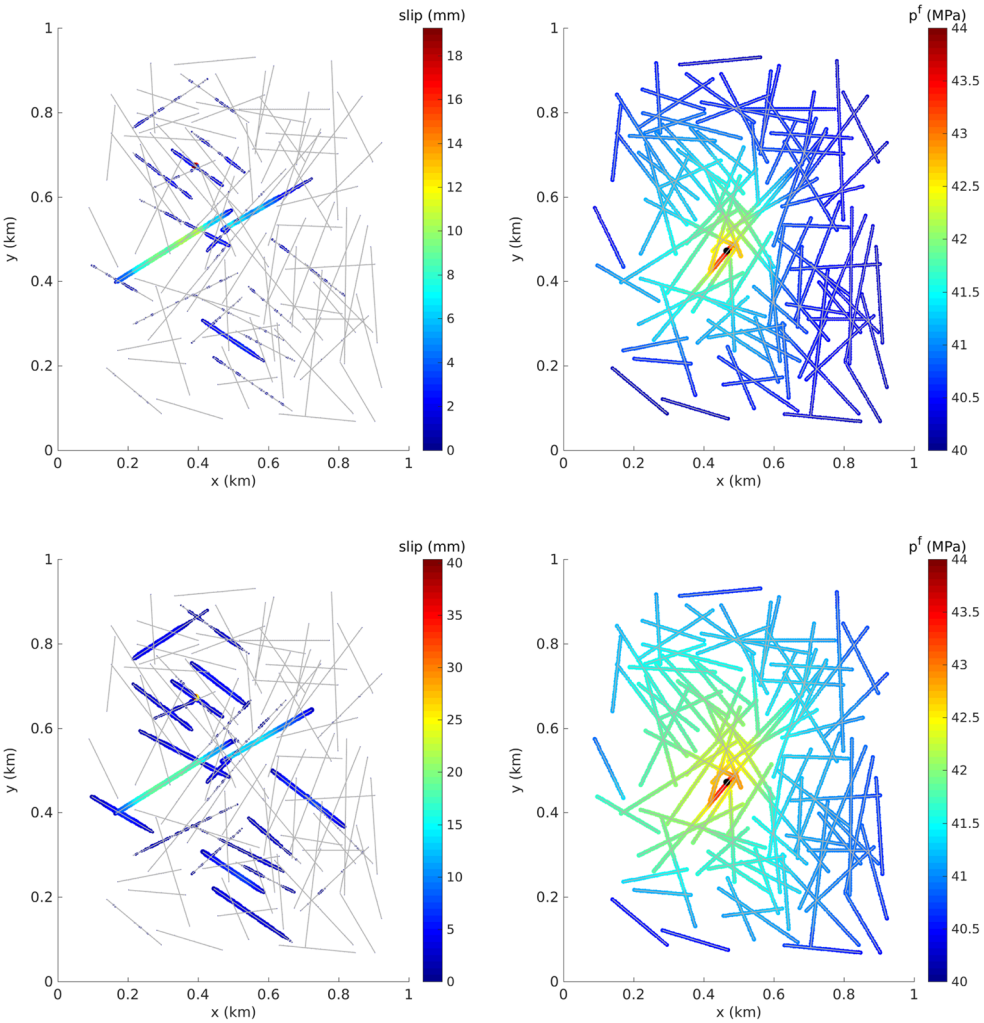


**Fig. 11** The slip solution (*left*) and pressure solution (*right*) after 800 s (in the *top row*) and 1600 s (in the *bottom row*) for the fracture network represented by *gray lines* in the *left* figure

be resolved. Therefore, it leads to diverging slip solutions for different grid resolutions. Diverging solutions are also obtained for hydraulic aperture, which directly depends on the shear slip. As a result, the fluid pressure solutions also diverge. This is an important consequence of slip-dependent aperture change. As compared to this solution, the shear strength relaxation model leads to grid convergent solutions for all three fields, i.e., slip, aperture, and fluid pressure in the fracture.

### 4.4 Fracture network

In order to test the numerical model for more realistic geological conditions, a fracture network with fluid injection is studied. The fractures are depicted as solid lines on the left of Fig. 11. The initial fluid pressure is 40 MPa everywhere and fluid injection occurs at the center with 44 MPa. The main model parameters are fracture length $L$, shear relaxation timescale $t_f$, static friction coefficient $\mu_s$, and fracture aperture $b^f$. Their probability density functions (PDF) are

$$f(L) = CL^{-2.1} \text{ for } L \in [0.17 \text{ km},\ 0.7 \text{ km}] \tag{25}$$

$$f\left(\log(t_f)\right) = \frac{1}{\sqrt{(2\pi\sigma_f^2)}} \exp\left(-\left(\log(t_f/t_0)\right)^2 \Big/ 2\sigma_f^2\right), \tag{26}$$

$$f(\mu_s) = \text{random}[\mu_a \quad \mu_b] \tag{27}$$

$$\text{and} \quad f(b^f) = \frac{1}{\sqrt{(2\pi\sigma_b^2)}} \exp\left(-\left(b^f - b_0\right)^2 / 2\sigma_b^2\right), \tag{28}$$

respectively, where Eq. 25 is taken from [17]. The elastic properties are kept fixed in these simulations. Heterogeneity of the friction coefficient plays a very important role for the micro-seismic behavior and heterogeneity of fracture aperture accounts for the varying flow resistance in the network. The figures in Fig. 11 depict pressure (right) and shear displacement (left) after two different time of simulations. The top row figures are for the initial stage of failure after 800 s and the bottom row figures are for simulations after 1600 s. It can be observed that at the initial stage, the fractures which are oriented to have least compressive and shear strength undergo failure first. Even though these fractures are not directly connected to the central well location (indicated by black dot on the right of Fig. 11), a very small pressure perturbation both via matrix and fracture fluid flow leads to these initial seismic activities. Eventually, the pressure build-up happens throughout the entire domain, and this leads to failure of other fractures as well, as depicted in the bottom row of Fig. 11. The simulation is based on the PDFs (26), (27), and (28) of $t_f$, $\mu_s$, and $b^f$, respectively. All required parameters are given in Table 1. The $b$-value curves of this fracture network, as depicted in the right plot of Fig. 9, follow the Gutenberg-Richter law for moment magnitudes greater than a specified minimum value. The latter was introduced, since a finite grid resolution does not allow for seismic moment estimation for arbitrarily small failing segments.The $b$-values are estimated for different grid resolutions. It can be observed that the $b$-value curves follow

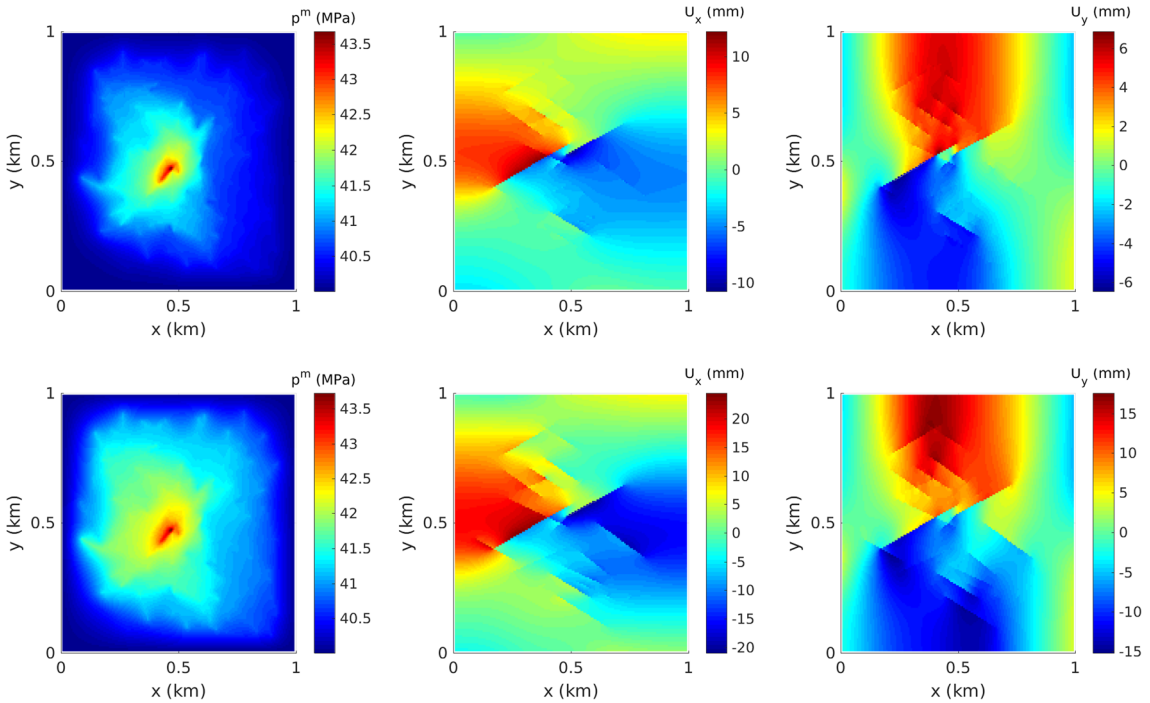


**Fig. 12** Matrix pressure and matrix displacement components $U_x$ and $U_y$ are shown after 800 s (in the *top row*) and 1600 s (in the *bottom row*) for the fracture network

a linear decay in both cases with approximately the same slope, which further confirms the convergence of the shear failure model presented in this paper.

Figure 12 depicts the matrix fluid pressure and the matrix displacement components after 800 s (in the top row) and 1600 s (in the bottom row) for the fracture network. For better visualization, displacement components are depicted relative to the initial displacement solution without any shear failure.

## 5 Conclusions

A numerical method is presented which can deal with fractures embedded in a damaged matrix. Shear slip, displacement, shear, and flow are consistently coupled, which allows to simulate flow induced shear failure. Thanks to a hierarchical fracture representation and discontinuity basis functions, the numerical method can be applied without conforming the grid around the fractures. Grid convergence of the shear relaxation model for the friction properties is demonstrated for fluid pressure, slip, and aperture. The method uses a poroelastic formulation for flow-mechanics coupling via a fixed stress approach.

The method was also used to study a fractured reservoir with heterogeneous friction properties, and it can be observed that micro-seismicity due to shear slip follows the Gutenberg-Richter law for moment magnitude. The results show grid-independent solutions for $b$-value slope for single fracture and fracture network problems.

**Acknowledgements** The work was performed as part of the GEOTHERM project that is funded by the Competence Center for Environment Sustainability of the ETH-Domain. The authors are grateful to Keith Evans, Dimitrios Karvounis, Timur Garipov, Nicola Castelletto, and Hamdi Tchelepi for the constructive remarks and suggestions during the course of the project.

## Appendix 1

The discretized (with the finite volume method) system of equations is described in this Appendix 1. An interaction region of matrix and fracture nodes is depicted in Fig. 13. Assuming that the discretization parameters are the same in both directions, the length of the square interaction region is $h = \triangle x = \triangle y$. The symbols $[e, w, n, s]$ indicate the bounding area of each finite volume segment within this interaction region, which contributes to the stress flux or force applied on each of the four interacting finite volume segments. The integrated stress can further be obtained from the integrated strain value along the boundary lines of each finite volume segment using the constitutive relation (2). In order to obtain the integrated strain field along the bounding

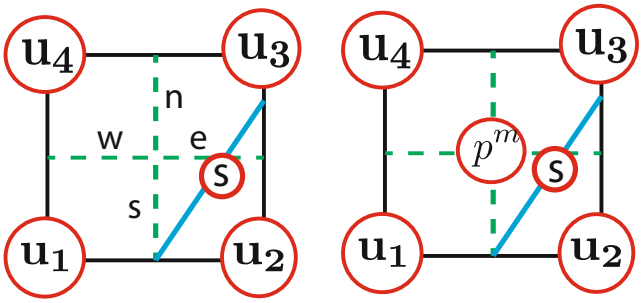


**Fig. 13** The illustration of the interaction region of basis functions along with the fracture dof and matrix dof. The *left* figure describes the interaction region for a mechanics problem with no poroelastic effects. The *right* figure depicts the location where matrix pressure node is stored for the poroelastic stress-strain relation

areas and the fracture line, a smooth displacement field is defined using bilinear basis functions corresponding to each matrix nodes. A local coordinate system is considered in this interaction region with origin at node $\mathbf{u_1}$. Using this local coordinate system, the bilinear basis functions corresponding to each of the four matrix nodes are given as follows:

$$N^1(x, y) = \left(1 - \frac{x}{h}\right)\left(1 - \frac{y}{h}\right), \tag{29}$$

$$N^2(x, y) = \frac{x}{h}\left(1 - \frac{y}{h}\right), \tag{30}$$

$$N^3(x, y) = \frac{x}{h}\frac{y}{h}, \text{ and} \tag{31}$$

$$N^4(x, y) = \frac{x}{h}\left(1 - \frac{y}{h}\right). \tag{32}$$

The integrated displacement derivative along the bounding areas of $[e, w, n, s]$, used in the strain estimation, can now be estimated using the basis functions and matrix node displacement dof as follows:

$$\begin{bmatrix} \mathbf{D_e^{x,x/y}} \\ \mathbf{D_w^{x,x/y}} \\ \mathbf{D_n^{x,x/y}} \\ \mathbf{D_s^{x,x/y}} \end{bmatrix} = \begin{bmatrix} (1/4) & (1/4) \\ (1/4) & (1/4) \\ (1/8) & (3/8) \\ (3/8) & (1/8) \end{bmatrix} \begin{bmatrix} (u_2^{x/y} - u_1^{x/y}) \\ (u_3^{x/y} - u_4^{x/y}) \end{bmatrix} \text{ and} \tag{33}$$

$$\begin{bmatrix} \mathbf{D_e^{y,x/y}} \\ \mathbf{D_w^{y,x/y}} \\ \mathbf{D_n^{y,x/y}} \\ \mathbf{D_s^{y,x/y}} \end{bmatrix} = \begin{bmatrix} (1/8) & (3/8) \\ (3/8) & (1/8) \\ (1/4) & (1/4) \\ (1/4) & (1/4) \end{bmatrix} \begin{bmatrix} (u_4^{x/y} - u_1^{x/y}) \\ (u_3^{x/y} - u_2^{x/y}) \end{bmatrix}. \tag{34}$$

In Eq. 33, the terms $\mathbf{D_e^{x,x/y}}$ and $\mathbf{D_e^{y,x/y}}$ are defined as follows:

$$\mathbf{D_e^{x,x/y}} = \int_e \frac{\partial u^{x/y}}{\partial x} dx \tag{35}$$

$$\text{and } \mathbf{D_e^{y,x/y}} = \int_e \frac{\partial u^{x/y}}{\partial y} dx. \tag{36}$$

The presence of a fracture line in the interaction region makes it necessary to define the displacement discontinuity due to shear slip along the fracture manifold, which is achieved with the discontinuity basis function (17). Using the bilinear basis functions (29), (30), (31), and (32), the contributions of each term $N_p^J(\mathbf{x})H_p^J(f^J(\mathbf{x}))$ for $p \in 1, 2, 3, 4$ are obtained and depicted on the left of Fig. 2. The full discontinuity basis function, i.e., the sum of the four individual contributions, is depicted on the right of Fig. 2. An important property of this discontinuity basis function is that its gradient is continuous across the fracture line. This allows to obtain the displacement derivative for this basis function in the limit of approaching the fracture line. This property therefore can be used to obtain the contribution of discontinuity dof in the force balance equation for each of the matrix node and in the force constraint equations along the fracture line. The contributions of displacement discontinuity to the integrated displacement derivative calculation along the bounding areas are given as follows:

$$\begin{bmatrix} \tilde{\mathbf{D}}_{\mathbf{e}}^{\mathbf{x},\mathbf{x}/\mathbf{y}} \\ \tilde{\mathbf{D}}_{\mathbf{w}}^{\mathbf{x},\mathbf{x}/\mathbf{y}} \\ \tilde{\mathbf{D}}_{\mathbf{n}}^{\mathbf{x},\mathbf{x}/\mathbf{y}} \\ \tilde{\mathbf{D}}_{\mathbf{s}}^{\mathbf{x},\mathbf{x}/\mathbf{y}} \end{bmatrix} = \begin{bmatrix} (t_{x/y}\mathbf{s}/4) & (t_{x/y}\mathbf{s}/4) \\ (t_{x/y}\mathbf{s}/4) & (t_{x/y}\mathbf{s}/4) \\ (t_{x/y}\mathbf{s}/8) & (3t_{x/y}\mathbf{s}/8) \\ (3t_{x/y}\mathbf{s}/8) & (t_{x/y}\mathbf{s}/8) \end{bmatrix} \begin{bmatrix} (H_2 - H_1) \\ (H_3 - H_4) \end{bmatrix} \text{ and} \tag{37}$$

$$\begin{bmatrix} \tilde{\mathbf{D}}_{\mathbf{e}}^{\mathbf{y},\mathbf{x}/\mathbf{y}} \\ \tilde{\mathbf{D}}_{\mathbf{w}}^{\mathbf{y},\mathbf{x}/\mathbf{y}} \\ \tilde{\mathbf{D}}_{\mathbf{n}}^{\mathbf{y},\mathbf{x}/\mathbf{y}} \\ \tilde{\mathbf{D}}_{\mathbf{s}}^{\mathbf{y},\mathbf{x}/\mathbf{y}} \end{bmatrix} = \begin{bmatrix} (t_{x/y}\mathbf{s}/8) & (3t_{x/y}\mathbf{s}/8) \\ (3t_{x/y}\mathbf{s}/8) & (t_{x/y}\mathbf{s}/8) \\ (t_{x/y}\mathbf{s}/4) & (t_{x/y}\mathbf{s}/4) \\ (t_{x/y}\mathbf{s}/4) & (t_{x/y}\mathbf{s}/4) \end{bmatrix} \begin{bmatrix} (H_4 - H_1) \\ (H_3 - H_2) \end{bmatrix}. \tag{38}$$

In Eq. 37, the terms $\tilde{\mathbf{D}}_{\mathbf{e},\mathbf{w},\mathbf{n},\mathbf{s}}^{\mathbf{x},\mathbf{x}/\mathbf{y}}$ represent the corrections of the integrated displacement derivative calculation due to shear slip. The first superscript $\mathbf{x}$ refers to to $x$ directional derivative. The second superscript $\mathbf{x}/\mathbf{y}$ refers to the $x$ or $y$ directional component of the displacement. Further, $H_p$, with $p \in \{1, 2, 3, 4\}$, represents the value of function (17) at any point within the interaction region excluding the fracture manifold. The variable $t_{x/y}$ represents the $x$ or $y$ directional component of the tangential vector along the fracture manifold. The variable $\mathbf{s}$ represents the shear slip discontinuity along the fracture manifold. Jointly, Eqs. 33, 34, 37, and 38 provide the contributions of each matrix node displacement and fracture node displacement to the discretized form of force balance Eq. 14.

The compressive and shear forces along the fracture manifold can be obtained using the integrated displacement derivative along the fracture line. The contributions of each matrix node to this integrated displacement derivative is given as follows:

$$\begin{bmatrix} \mathbf{D}_{\mathbf{L}}^{\mathbf{x},\mathbf{x}/\mathbf{y}} \\ \mathbf{D}_{\mathbf{L}}^{\mathbf{y},\mathbf{x}/\mathbf{y}} \end{bmatrix} = \begin{bmatrix} (L/h)\left(1 - (C_y/h)\right) & 0 \\ (C_y L/h^2) & 0 \\ 0 & (L/h)\left(1 - (C_x/h)\right) \\ 0 & (C_x L/h^2) \end{bmatrix}^T \begin{bmatrix} (u_2^{x/y} - u_1^{x/y}) \\ (u_3^{x/y} - u_4^{x/y}) \\ (u_4^{x/y} - u_1^{x/y}) \\ (u_3^{x/y} - u_2^{x/y}) \end{bmatrix}. \tag{39}$$

In Eq. 39, the term $\mathbf{D}_{\mathbf{L}}^{\mathbf{x},\mathbf{x}/\mathbf{y}}$ represents the integrated value of the derivative with respect to $x$ for the displacement components in $x$ or $y$ direction. The variables $L$, $C_x$, and $C_y$ respectively represent the length of the fracture segment, and the local $x$ and $y$ coordinates of the fracture centre within the interaction region. Equation 39 is used to calculate the integrated compressive and shear traction forces on the fracture manifold. The correction of the integrated displacement derivative calculation along the fracture segment due to the discontinuity dof is obtained as follows:

$$\begin{bmatrix} \tilde{\mathbf{D}}_{\mathbf{L}}^{\mathbf{x},\mathbf{x}/\mathbf{y}} \\ \tilde{\mathbf{D}}_{\mathbf{L}}^{\mathbf{y},\mathbf{x}/\mathbf{y}} \end{bmatrix} = \begin{bmatrix} (L/h)\left(1 - (C_y/h)\right)(t_{x/y}\mathbf{s}) & 0 \\ (C_y L/h^2)(t_{x/y}\mathbf{s}) & 0 \\ 0 & (L/h)\left(1 - (C_x/h)\right)(t_{x/y}\mathbf{s}) \\ 0 & (C_x L/h^2)(t_{x/y}\mathbf{s}) \end{bmatrix}^T \begin{bmatrix} (H_2 - H_1) \\ (H_3 - H_4) \\ (H_4 - H_1) \\ (H_3 - H_2) \end{bmatrix}. \tag{40}$$

Jointly, Eqs. 39 and 40 provide the contribution of each matrix and fracture node displacement to the discretized form of force constraint Eq. 13. Together, force balance and force constraint equation constitute the linear system to be solved for matrix and fracture displacement dof. In the poroelastic domain, the matrix pressure $p^m$ also contributes to the poroelastic constitutive stress-strain relation (8). The matrix pressure values of the coupled flow-mechanics system are represented between the matrix displacement nodes, as depicted on the right of Fig. 13. This results in a staggered grid approach with different nodes for matrix pressure and displacement values. Further, the displacement divergence calculation in the discretized form of Eq. 9 is obtained using the displacement basis functions, matrix displacement dof, and fracture displacement discontinuity dof.

Figure 14 depicts an illustration of deriving the discretized force balance equation for the displacement $u_{11}$ at a node. The use of bilinear basis functions lead to a 9-point stencil for the central node. In order to obtain the applied forces at the volume boundaries, the stress components are integrated along the green dotted line. Using Eq. 2, the stress components can be replaced by integrated displacement derivatives along the volume boundaries. The integrated value of displacement derivative corresponding to an interaction region is marked with the subscript **ij**, which indicates the south western node of the interaction region. As an example, the contribution to the integrated value of the displacement derivative along the southern green dotted line, due to the four corner matrix node dofs, in the interaction region with the south western node $u_{11}$ is denoted by $\mathbf{D}^{\mathbf{x/y,x/y}}_{\mathbf{s,11}}$. The contribution of shear slip in the calculation of the displacement derivative for the same line is denoted by $\tilde{\mathbf{D}}^{\mathbf{x/y,x/y}}_{\mathbf{s,11}}$. The integrated form of force balance (14) in each $x$ and $y$ direction (for a $2D$ problem) is obtained as follows:

$$\int_{d\Omega}(\tilde{\sigma}_{xx}-bp)\,dy+\int_{d\Omega}\tilde{\sigma}_{xy}dx+\int_{\Omega}f_x d\Omega=0 \text{ and } (41)$$

$$\int_{d\Omega}(\tilde{\sigma}_{yy}-bp)\,dx+\int_{d\Omega}\tilde{\sigma}_{xy}dy+\int_{\Omega}f_y d\Omega=0, \quad (42)$$

where $\tilde{\sigma}_{ij}$ represents the individual components of the effective stress tensor $\tilde{\sigma}$. The terms $f_x$ and $f_y$, in Eqs. 41 and (42), respectively, represent the individual components of the body force **f**. Further, replacing the effective stress term using the stress-strain relation (2), the force balance is given as

$$\int_{d\Omega}\left((\lambda+2G)\frac{\partial u_x}{\partial x}+\lambda\frac{\partial u_y}{\partial y}-bp\right)dy + \int_{d\Omega}G\left(\frac{\partial u_x}{\partial y}+\frac{\partial u_y}{\partial x}\right)dx+\int_{\Omega}f_x d\Omega=0 \text{ and} \quad (43)$$

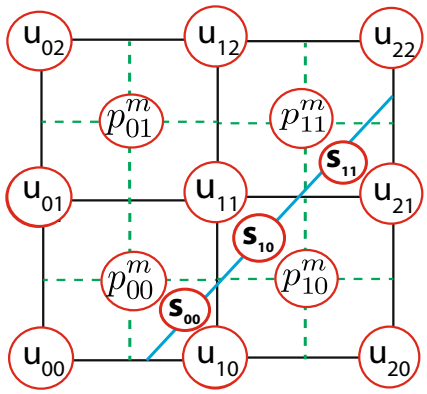


**Fig. 14** The illustration of 9-point stencil for the finite volume discretization of force balance equations for the displacement node marked as $u_{11}$

$$\int_{d\Omega}\left((\lambda+2G)\frac{\partial u_y}{\partial y}+\lambda\frac{\partial u_x}{\partial x}-bp\right)dx + \int_{d\Omega}G\left(\frac{\partial u_x}{\partial y}+\frac{\partial u_y}{\partial x}\right)dy+\int_{\Omega}f_y d\Omega=0. \quad (44)$$

Replacing each of the displacement derivatives with the integrated form for the rectangular boundary surrounding the center node, the force balance equation in $x$ direction is obtained as follows:

$$\begin{aligned}&(\lambda+2G)\left(\mathbf{D}^{\mathbf{x,x}}_{\mathbf{s,11}}+\tilde{\mathbf{D}}^{\mathbf{x,x}}_{\mathbf{s,11}}-\mathbf{D}^{\mathbf{x,x}}_{\mathbf{s,01}}\right)+\lambda\left(\mathbf{D}^{\mathbf{y,y}}_{\mathbf{s,11}}+\tilde{\mathbf{D}}^{\mathbf{y,y}}_{\mathbf{s,11}}-\mathbf{D}^{\mathbf{y,y}}_{\mathbf{s,01}}\right)\\&+(\lambda+2G)\left(\left(\mathbf{D}^{\mathbf{x,x}}_{\mathbf{n,10}}+\tilde{\mathbf{D}}^{\mathbf{x,x}}_{\mathbf{n,10}}\right)-\left(\mathbf{D}^{\mathbf{x,x}}_{\mathbf{n,00}}+\tilde{\mathbf{D}}^{\mathbf{x,x}}_{\mathbf{n,00}}\right)\right)\\&+\lambda\left(\left(\mathbf{D}^{\mathbf{y,y}}_{\mathbf{n,10}}+\tilde{\mathbf{D}}^{\mathbf{y,y}}_{\mathbf{n,10}}\right)-\left(\mathbf{D}^{\mathbf{y,y}}_{\mathbf{n,00}}+\tilde{\mathbf{D}}^{\mathbf{y,y}}_{\mathbf{n,00}}\right)\right)\\&+G\left(\left(\mathbf{D}^{\mathbf{x,y}}_{\mathbf{w,11}}+\tilde{\mathbf{D}}^{\mathbf{x,y}}_{\mathbf{w,11}}\right)-\left(\mathbf{D}^{\mathbf{x,y}}_{\mathbf{w,10}}+\tilde{\mathbf{D}}^{\mathbf{x,y}}_{\mathbf{w,10}}\right)+\left(\mathbf{D}^{\mathbf{y,x}}_{\mathbf{w,11}}+\tilde{\mathbf{D}}^{\mathbf{y,x}}_{\mathbf{w,11}}\right)-\left(\mathbf{D}^{\mathbf{y,x}}_{\mathbf{w,10}}+\tilde{\mathbf{D}}^{\mathbf{y,x}}_{\mathbf{w,10}}\right)\right)\\&+G\left(\mathbf{D}^{\mathbf{x,y}}_{\mathbf{e,01}}-\left(\mathbf{D}^{\mathbf{x,y}}_{\mathbf{e,00}}+\tilde{\mathbf{D}}^{\mathbf{x,y}}_{\mathbf{e,00}}\right)+\mathbf{D}^{\mathbf{y,x}}_{\mathbf{e,01}}-\left(\mathbf{D}^{\mathbf{y,x}}_{\mathbf{e,00}}+\tilde{\mathbf{D}}^{\mathbf{y,x}}_{\mathbf{e,00}}\right)\right)\\&+0.5b\Delta y\left((p^m_{01}+p^m_{00})-(p^m_{11}+p^m_{10})\right)+f_x\Delta V=0.\end{aligned} \quad (45)$$

Similarly, the force balance equation in $y$-direction is obtained as follows:

$$\begin{aligned}&(\lambda+2G)\left(\left(\mathbf{D}^{\mathbf{y,y}}_{\mathbf{w,11}}+\tilde{\mathbf{D}}^{\mathbf{y,y}}_{\mathbf{w,11}}\right)-\left(\mathbf{D}^{\mathbf{y,y}}_{\mathbf{w,10}}+\tilde{\mathbf{D}}^{\mathbf{y,y}}_{\mathbf{w,10}}\right)+\mathbf{D}^{\mathbf{y,y}}_{\mathbf{e,01}}-\left(\mathbf{D}^{\mathbf{y,y}}_{\mathbf{e,00}}+\tilde{\mathbf{D}}^{\mathbf{y,y}}_{\mathbf{e,00}}\right)\right)\\&+\lambda\left(\left(\mathbf{D}^{\mathbf{x,x}}_{\mathbf{w,11}}+\tilde{\mathbf{D}}^{\mathbf{x,x}}_{\mathbf{w,11}}\right)-\left(\mathbf{D}^{\mathbf{x,x}}_{\mathbf{w,10}}+\tilde{\mathbf{D}}^{\mathbf{x,x}}_{\mathbf{w,10}}\right)+\mathbf{D}^{\mathbf{x,x}}_{\mathbf{e,01}}-\left(\mathbf{D}^{\mathbf{x,x}}_{\mathbf{e,00}}+\tilde{\mathbf{D}}^{\mathbf{x,x}}_{\mathbf{e,00}}\right)\right)\\&+G\left(\left(\mathbf{D}^{\mathbf{x,y}}_{\mathbf{s,11}}+\tilde{\mathbf{D}}^{\mathbf{x,y}}_{\mathbf{s,11}}\right)-\mathbf{D}^{\mathbf{x,y}}_{\mathbf{s,01}}+\left(\mathbf{D}^{\mathbf{y,x}}_{\mathbf{s,11}}+\tilde{\mathbf{D}}^{\mathbf{y,x}}_{\mathbf{s,11}}\right)-\mathbf{D}^{\mathbf{y,x}}_{\mathbf{s,01}}\right)\\&+G\left(\left(\mathbf{D}^{\mathbf{x,y}}_{\mathbf{n,10}}+\tilde{\mathbf{D}}^{\mathbf{x,y}}_{\mathbf{n,10}}\right)-\left(\mathbf{D}^{\mathbf{x,y}}_{\mathbf{s,00}}+\tilde{\mathbf{D}}^{\mathbf{x,y}}_{\mathbf{s,00}}\right)+\left(\mathbf{D}^{\mathbf{y,x}}_{\mathbf{n,10}}+\tilde{\mathbf{D}}^{\mathbf{y,x}}_{\mathbf{n,10}}\right)-\left(\mathbf{D}^{\mathbf{y,x}}_{\mathbf{s,00}}+\tilde{\mathbf{D}}^{\mathbf{y,x}}_{\mathbf{s,00}}\right)\right)\\&+0.5b\Delta x\left((p^m_{10}+p^m_{00})-(p^m_{11}+p^m_{01})\right)+f_x\Delta V=0.\end{aligned} \quad (46)$$

$\Delta V$ in Eqs. 45 and 46 is the area of the rectangular region surrounding the center node. It has to be mentioned that the additional contribution to the integrated value of the displacement derivative $\left(\tilde{\mathbf{D}}^{\mathbf{x/y,x/y}}_{\mathbf{e/w/n/s,ij}}\right)$ appears in the discretized force balance (45) and (46) only if the interaction region contains a fracture manifold dof. Using the constitutive relation (2) and (3b) in Eq. 13, the force constraint relation becomes

$$G\left(n_y^2-n_x^2\right)\int_0^L\left(\frac{\partial u_y}{\partial x}+\frac{\partial u_x}{\partial y}\right) + 2Gn_xn_y\int_0^L\left(\frac{\partial u_x}{\partial x}-\frac{\partial u_y}{\partial y}\right)=\int_0^L\tau_{\max}, \quad (47)$$

where $n_x$ and $n_y$ respectively represent the $x$ and $y$ directional component of unit vector $\hat{n}$, normal to the fracture manifold. Using the integrated value of the displacement derivative along the fracture manifold, the force constraint equation for a fracture segment in the interaction region with the south western grid node $X_{ij}$ is obtained as follows:

$$\begin{aligned}&G\left(n_y^2-n_x^2\right)\left(\left(\mathbf{D}^{\mathbf{x,y}}_{\mathbf{L,ij}}+\tilde{\mathbf{D}}^{\mathbf{x,y}}_{\mathbf{L,ij}}\right)+\left(\mathbf{D}^{\mathbf{y,x}}_{\mathbf{L,ij}}+\tilde{\mathbf{D}}^{\mathbf{y,x}}_{\mathbf{L,ij}}\right)\right)\\&+2Gn_xn_y\left(\left(\mathbf{D}^{\mathbf{x,x}}_{\mathbf{L,ij}}+\tilde{\mathbf{D}}^{\mathbf{x,x}}_{\mathbf{L,ij}}\right)-\left(\mathbf{D}^{\mathbf{y,y}}_{\mathbf{L,ij}}+\tilde{\mathbf{D}}^{\mathbf{y,y}}_{\mathbf{L,ij}}\right)\right)=L\tau_{\max}.\end{aligned} \quad (48)$$

In the finite volume formulation, the mass balance (9) is integrated over a finite volume segment centered around each pressure node. The integrated mass balance equation for a discretized finite volume $\Omega$ is given as follows:

$$\frac{1}{M}\frac{\partial\left(\int_{\Omega} p^m d\Omega\right)}{\partial t} + b\frac{\partial\left(\int_{d\Omega}\mathbf{u}\cdot d\mathbf{A}\right)}{\partial t} - \int_{d\Omega}\left(\frac{\boldsymbol{\kappa}^{\boldsymbol{m}}}{\mu}\cdot\nabla p^m\right)\cdot d\mathbf{A} + \int_{\Omega}\left(\Psi^{m\to f} - q^m\right)d\Omega = 0. \quad (49)$$

For the rectangular finite volume centered around the pressure node $X^m_{11}$, the Eq. 49 simplified to

$$\frac{\Delta V}{M}\frac{dp^m_{11}}{dt} + b\frac{d}{dt}\left(\sum_{fc}\mathbf{u}\cdot\Delta\mathbf{A}\right) - \sum_{fc}\left(\frac{\boldsymbol{\kappa}^{\boldsymbol{m}}}{\mu}\cdot\nabla p^m\right)\cdot\Delta\mathbf{A} + \left(C^{mf}\left(p^m_{11} - p^f_{11}\right) - q^m\right)\Delta V = 0, \quad (50)$$

where $C^{mf}$ is the mass transfer coefficient between matrix volume and the fracture segment, and $fc$ represents a rectangular boundary line for the finite volume centered around the node $X^m_{11}$. The use of bilinear basis functions simplifies the area integral of the displacement calculation along a rectangular boundary to $\mathbf{u}\cdot\Delta\mathbf{A}$, where $\mathbf{u}$ is the displacement average of the nodes connecting the boundary line. The integration of the discontinuity basis function (17) along the boundary is zero. Therefore, the shear slip dof has no direct contribution to the discretized mass balance (50). Details of mass balance equation for the fracture manifold can be obtained from [18] and details of $C^{mf}$ can be found in [2].

The displacement derivative terms in the discretized force balance (45) and (46), and the force constraint relation (48) are replaced using Eqs. 33, 34, 37, 38, 39, and 40 to obtain the final force balance and force constraint equations in terms of matrix displacement dof, matrix pressure dof and shear slip dof which are given as follows:

$$\tilde{\mathbf{K}}_{xx}\mathbf{U}_x + \tilde{\mathbf{K}}_{xy}\mathbf{U}_y + \tilde{\mathbf{C}}_{xs}\mathbf{S} = \mathbf{B}_x - \tilde{\mathbf{C}}_{xm}\mathbf{P}^{\mathbf{m}}, \quad (51)$$

$$\tilde{\mathbf{K}}_{xy}\mathbf{U}_x + \tilde{\mathbf{K}}_{yy}\mathbf{U}_y + \tilde{\mathbf{C}}_{ys}\mathbf{S} = \mathbf{B}_y - \tilde{\mathbf{C}}_{ym}\mathbf{P}^{\mathbf{m}}, \quad (52)$$

$$\text{and } \tilde{\mathbf{C}}_{ss}\mathbf{S} + \tilde{\mathbf{C}}_{sx}\mathbf{U}_x + \tilde{\mathbf{C}}_{sy}\mathbf{U}_y = \mathbf{B}_s, \quad (53)$$

where each matrix $\tilde{\mathbf{K}}_{ij}$ accounts for the contribution of the displacment gradient component in $j$-direction for the force balance in $i$-direction. The matrices $\tilde{\mathbf{C}}_{xs}$ and $\tilde{\mathbf{C}}_{ys}$ account for the contribution of shear slip in the calculation of the integrated displacement derivative given as $\tilde{\mathbf{D}}^{\mathbf{x/y,x/y}}_{\mathbf{e/w/n/s,ij}}$. The matrices $\tilde{\mathbf{C}}_{xm}$ and $\tilde{\mathbf{C}}_{ym}$ account for the contribution of matrix pressure in the calculation of force balance (45) and (46). The matrix $\tilde{\mathbf{C}}_{ss}$ in Eq. 53 corresponds to the contribution of shear slip in the calculation of the integrated displacement derivative along the fracture manifold $\left(\tilde{\mathbf{D}}^{\mathbf{x/y,x/y}}_{\mathbf{L,ij}}\right)$. Finally, the matrices $\tilde{\mathbf{C}}_{sx}$ and $\tilde{\mathbf{C}}_{sy}$ in Eq. 53 account for the contribution of $x$ and $y$ directional matrix displacement components in the calculation of the integrated displacement derivative along the fracture manifold $\left(\mathbf{D}^{\mathbf{x/y,x/y}}_{\mathbf{L,ij}}\right)$. The discretized mass balance equations for the matrix and the fracture manifolds in terms of matrix and fracture dofs are given as follows:

$$\tilde{\mathbf{M}}_{mm}\mathbf{P}_m + \tilde{\mathbf{M}}_{fm}\mathbf{P}_f = \mathbf{B}_m - \tilde{\mathbf{M}}_{mx}\mathbf{U}_x - \tilde{\mathbf{M}}_{my}\mathbf{U}_y \quad (54)$$

$$\text{and } \tilde{\mathbf{M}}_{ff}\mathbf{P}_f + \tilde{\mathbf{M}}_{mf}\mathbf{P}_m = \mathbf{B}_f. \quad (55)$$

The matrices $\tilde{\mathbf{M}}_{mm}$ and $\tilde{\mathbf{M}}_{ff}$ corresponds to the contribution of the matrix pressure node and fracture dofs in the discretized mass balance equations for matrix and fracture node, respectively. The matrices $\tilde{\mathbf{M}}_{fm}$ and $\tilde{\mathbf{M}}_{mf}$ account for mass transfer between discretized matrix finite volume and the fracture manifold. The matrices $\tilde{\mathbf{M}}_{mx}$ and $\tilde{\mathbf{M}}_{my}$ account for the contribution of matrix displacement nodes in the calculation of volumetric strain in the discretized mass balance (50). Trilinos $ML$ package [19] has been used to solve this coupled system using the fixed stress approach for the sequential solution of pressure and displacement values.

## Appendix 2

The dipping fault solutions using Volterra's formula provide analytical solutions for free surface displacement components due to a constant displacement discontinuity along a fault placed at a depth $d$ with a dip angle $\delta$ with respect to horizontal and a width $w$. This solution is used to

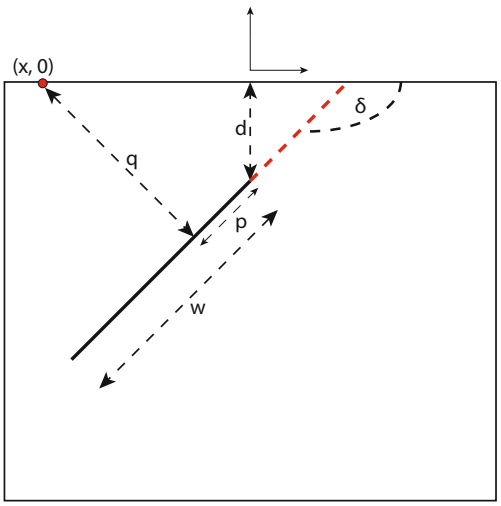


**Fig. 15** The figures depicts the set-up for the analytical dipping fault solution using Volterra's formula

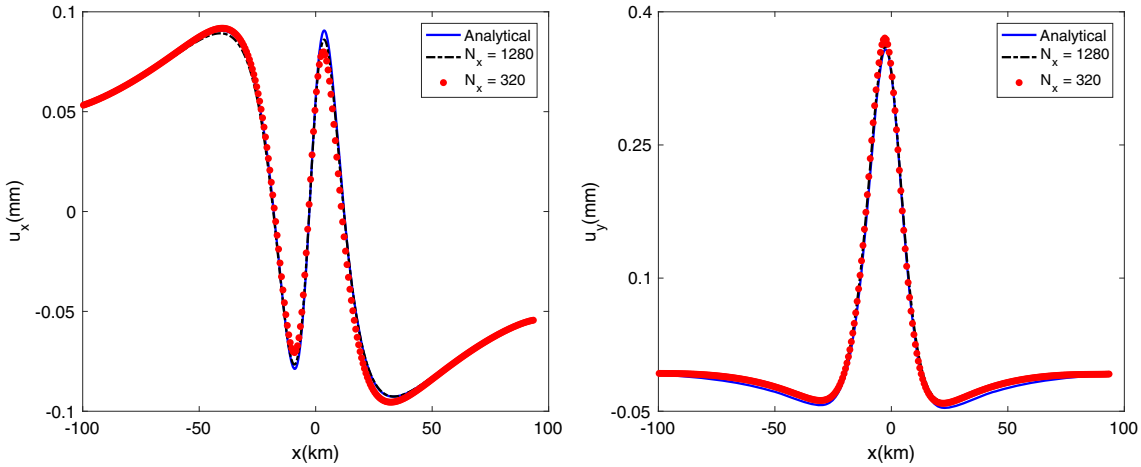


**Fig. 16** The figures depict comparison between numerical and analytical solutions of free surface displacement due to a fault placed at a depth of $d$ with dip angle $\delta$ and width $w$

provide a benchmark for the numerical solutions imposed by a constant shear slip along the fault using XFVM. Figure 15 provides the set-up for the simulation. The values of $d$, $\delta$, and $w$ are respectively 11.87 km, $135^0$, and 8.84 km. Free surface at the upper and lower domain boundaries and the anlytical displacement values at the top left and right corners are applied. The analytical solution decays linearly to zero at the bottom left and right corners of the domain. The analytical solution is obtained from [20] as

$$F(\eta) = \left[\cos\delta \tan^{-1}\left(\frac{\eta}{q}\right) - \left(\frac{q\eta\cos\delta + q^2\sin\delta}{q^2+\eta^2}\right)\right], \quad (56)$$

$$G(\eta) = \left[\sin\delta \tan^{-1}\left(\frac{\eta}{q}\right) + \left(\frac{q^2\cos\delta - q\eta\sin\delta}{q^2+\eta^2}\right)\right], \quad (57)$$

$$u_x = -\frac{s}{\pi}\left(F(p-w) - F(p)\right) \text{ and} \quad (58)$$

$$u_y = \frac{s}{\pi}\left(G(p-w) - G(p)\right). \quad (59)$$

Here, the variable $q$ represents the normal distance from a point $(x, 0)$ on the surface to the fault manifold. In Eqs. 56 and 57, the term $\eta$ represents a function variable. The variable $p$ represents the signed distance from the upper end of the fault to the projection of the point $(x, 0)$ on the fault manifold.

Figure 16 compares the numerical results for two different grid resolutions with the analytical solution of the displacement components. The numerical solutions converge to the analytical one with increasing grid resolution. These results verify the use of XFVM to obtain fracture slip-dependent displacement solutions.

## References


1. Lee, S.H., Lough, M.F., Jensen, C.L.: Water Resour. Res. **37**(3), 443 (2001)
2. Hajibeygi, H., Karvounis, D., Jenny, P.: J. Comput. Phys. **230**, 8729 (2011)
3. Karvounis, D.: Simulations of Enhanced Geothermal Systems with an Adaptive Hierarchical Fracture Representation, PhD Thesis (ETH Zurich) (2013)
4. Liu, F., Borja, R.I.: Comput. Methods Appl. Mech. Eng. **199**(37), 2456 (2010)
5. Prevost, J.H., Sukumar, N.: J. Mech. Phys. Solids **86**, 1 (2016)
6. Foster, C.D., Borja, R.I., Regueiro, R.A.: International Journal for Numerical and Analytical Methods in Engineering **72**(5), 549 (2007)
7. Rethore, J., De Borst, R., Abellan, M.A.: Comput. Mech. **42**(2), 227 (2008)
8. Deb, R., Jenny, P.: doi:10.1002/nag.2707 (2017)
9. Kim, J., Tchelepi, H.A., Juanes, R.: Comput. Methods Appl. Mech. Eng. **200**, 1591 (2011)
10. Scuderi, M.M., Carpenter, B.M., Johnson, P.A., Marone, C.: J. Geophys. Res. Solid Earth **120**, 6895 (2015)
11. Kammer, D.: Slip fronts at frictional interfaces: A Numerical and Theoretical Study, PhD Thesis (EPFL Lausanne (2014)
12. Prakash, V., Clifton, R.J.: Experimental techniques in the dynamics of deformable solids. ASME **165**, 33 (1993)
13. Rice, J.: J. Geophys. Res. **98**, 9885 (1993)
14. McClure, M., Horne, R.: Geophysics **76**(6), 181 (2011)
15. Castelletto, N., White, J.A., Tchelepi, H.A.: Int. J. Numer. Anal. Methods Geomech. **39**, 1593 (2015)
16. Hanks, T., Kanamori, H.: J. Geophys. Res. **84**(B5), 2348 (1979)
17. Rahman, M.K., Hossain, M.M., Rahman, S.S.: Int. J. Numer. Anal. Methods Geomech. **26**, 469 (2002)
18. Karvounis, D., Jenny, P.: Multiscale Model. Simul. **14**(1), 207 (2016)
19. Gee, M., Siefert, C., Hu, J., Tuminaro, R., Sala, M.: ML 5.0 Smoothed aggregation user's guide. Tech. Rep. SAND2006-2649, Sandia National Laboratories (2006)
20. Segall, P.: Earthquake and volcano deformation. Princeton University Press, Princeton (2010)